

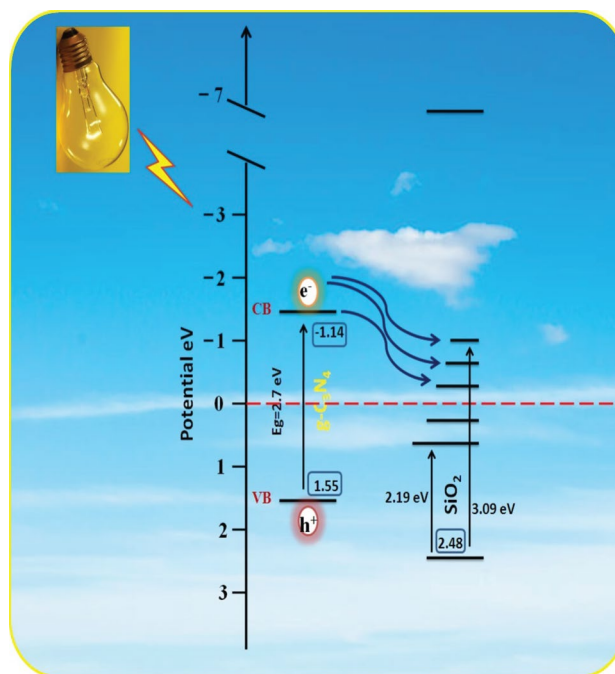
Design and Fabrication of a Novel Metal-Free SiO₂/g-C₃N₄ Nanocomposite: A Robust Photocatalyst for the Degradation of Organic Contaminants

K. Prakash¹ · P. Senthil Kumar¹ · P. Latha¹ · K. Saravanakumar¹ · S. Karuthapandian¹

Received: 24 August 2017 / Accepted: 20 October 2017 / Published online: 26 October 2017
© Springer Science+Business Media, LLC 2017

Abstract Development of novel and efficient nanostructured materials for the waste water treatment is a great challenge for the researchers. In this regard, we report a novel SiO₂/g-C₃N₄ nanocomposites were tailored via simple solvothermal route and characterized by various spectroscopic and microscopic techniques such as XRD, FT-IR, UV–Vis DRS, SEM, TEM and XPS. The photocatalytic performances of the as-prepared SiO₂/g-C₃N₄ nanocomposites were evaluated for the removal of hazardous rhodamine B (RhB) and crystal violet (CV) organic dyes in aqueous solution under visible light irradiation. Interestingly, the UV–Visible spectroscopy results revealed that the as-synthesized SiO₂/g-C₃N₄ nanocomposite showed superior photocatalytic activity for the degradation of RhB and CV dyes could degrade 99 and 98% under visible-light irradiation respectively. The enhanced photocatalytic activity of SiO₂/g-C₃N₄ nanocomposites could be mainly attributed to the proficient separation of photo-induced charge carriers. A plausible degradation mechanism for the controlled visible-light photocatalytic activity of SiO₂/g-C₃N₄ nanocomposites was strongly evidenced by the trapping experiment by employing different scavengers. The present research findings may open up a new platform for the g-C₃N₄ based photocatalyst for the degradation of organic pollutants.

Graphical Abstract Proposed degradation mechanism of the SiO₂/g-C₃N₄ photocatalyst.



Keywords SiO₂/g-C₃N₄ nanocomposite · Solvothermal synthesis · Visible-light photocatalyst · Scavenger

Electronic supplementary material The online version of this article (doi:10.1007/s10904-017-0715-5) contains supplementary material, which is available to authorized users.

✉ S. Karuthapandian
drpandianskvhnsnc2007@gmail.com

¹ Department of Chemistry, VHNSN College, Virudhunagar, Tamil Nadu 626001, India

1 Introduction

In these days, the release of dangerous pollutants into the environment is increasing due to the rapid development of industries which cause deaths and numerous numbers of

diseases to the human beings. The release of waste waters from the industries contains huge amounts of inorganic and organic pollutants [1, 2]. The present major organic pollutants such as aromatic hydrocarbons, polychlorinated biphenyls (PCBs), sulphonamides, dyestuff, aromatic nitro compounds, and phenols can give the serious problem to the ecosystems and human health because of their toxic and carcinogenic nature [3]. Especially, above 0.7 millions of colored organic dyes discharged into the aquatic system by leather, plastic, cosmetic and textile industries in each year which also causes negative impact of the living things [4]. Therefore, detoxification of hazardous dyes is an important concern to save the living organisms from diseases. Various techniques including adsorption, coagulation, ultrafiltration, reverse osmosis and photocatalysis have been used for the waste water treatment [5]. Among them, photocatalysis could offer simple, inexpensive and eco-friendly route for the treatment of toxic organic and inorganic pollutants containing wastewater [6, 7]. TiO_2 is one of the good photocatalyst materials due to the excellent photostability, low cost and non-toxicity. However, unfortunately TiO_2 is active only in the UV-light region and it may restrict the potential applications. There are several efforts have been made to develop the photocatalytic performance by tuning the properties of the photocatalyst.

Recently, non-metal π -conjugated polymeric graphitic carbon nitride ($\text{g-C}_3\text{N}_4$) an n-type organic semiconductor material have been widely investigated due to their peculiar properties such as thermal stability, inexpensive, low cost, reusability, nontoxic, molecular tunability, optoelectronic property and visible light responsive nature [8–10], and therefore used as an gas sensor [11], oxygen reduction reaction (ORR) [12], fuel cell [13], metal–organic frameworks (MOFs) [14], supercapacitors [15] and photocatalysis [16]. Conversely, the photocatalytic properties of $\text{g-C}_3\text{N}_4$ limits for its practical applications due to the high recombination rate of photogenerated e^- – h^+ pairs [17]. Numerous of attempts have been developed to conquer this problem and enhance the photocatalytic performance of $\text{g-C}_3\text{N}_4$. Several ways can be attempted including structure modification, constructing hetero junctions [18, 19], doping with metal-free or metal elements [20–22], and coupling with metals [23] and so on. Among the above, construction of semiconductor heterostructure is one of the greatest choice to slow down the photoinduced charge carriers and enriches the photocatalytic activity and stability [24]. Silicon dioxide (SiO_2) as a p-type anode metalloid or mesoporous materials have drawn much attention in recent years because of their superior properties viz excellent thermal stability, low cost, environmental-friendly, large surface area, chemical inertness, high thermal conductivity, good transparency and slow down discharge potential [25–27]. SiO_2 has been widely used in many suitable applications such as catalysts [28], Li-ion battery [29],

sensors [30], drug delivery and anti-caking agent [31, 32]. Recently, $\text{TiO}_2/\text{g-C}_3\text{N}_4$ [33, 34], graphene/ $\text{g-C}_3\text{N}_4$ [35], $\text{ZnO}/\text{g-C}_3\text{N}_4$ [36], $\text{MoS}_2/\text{g-C}_3\text{N}_4$ [37], $\text{Bi}_2\text{WO}_6/\text{g-C}_3\text{N}_4$ [38] are supported photocatalysts have shown stupendous photocatalytic properties compared with the metal-free $\text{g-C}_3\text{N}_4$ photocatalyst. Nevertheless, doping of SiO_2 with $\text{g-C}_3\text{N}_4$ may stronger and increase the visible light absorption range and overdue the recombination rate of photoexcited charge carriers. Up to our literature survey, there are no reports available on the synthesis of $\text{SiO}_2/\text{g-C}_3\text{N}_4$ nanocomposite and utilized as a photocatalyst for the degradation of environmental hazardous RhB and CV dyes.

With this mind, we made an attempt to the fabrication of $\text{SiO}_2/\text{g-C}_3\text{N}_4$ nanocomposite via simple solvothermal method for the first time. The successful formation of $\text{SiO}_2/\text{g-C}_3\text{N}_4$ nanocomposites was confirmed by various analytical and spectroscopic techniques such as XRD, FTIR, SEM, TEM, UV, PL and XPS. The as-prepared $\text{SiO}_2/\text{g-C}_3\text{N}_4$ nanocomposites were employed as a photocatalyst for the degradation of environmentally toxic and widely used toxic RhB and CV dye solution. Based on the trapping experiment results, we have explored a plausible photodegradation mechanism for the superior photocatalytic activity of $\text{SiO}_2/\text{g-C}_3\text{N}_4$.

2 Experimental Section

2.1 Material

All the reagents were of analytical grade and were used without further purification. We purchased the chemicals from Merck specialities Private Limited, Mumbai, India. Double distilled water was used throughout the experiment.

2.2 Synthesis of $\text{g-C}_3\text{N}_4$

The metal-free $\text{g-C}_3\text{N}_4$ was synthesized according to the previously reported method [39]. In a typical synthesis, 1.253 g of melamine was dissolved in 35 mL of ethylene glycol and addition of 50 mL of 0.1 M HNO_3 was slowly added and the mixture was constant stirring for 1 h. The resulting suspension mixture was washed with double distilled water and ethanol for several times, and dried at 60 °C for 12 h. Then, the white color powder was annealed at 550 °C for 4 h at heating rate of 10 °C/min. Finally, $\text{g-C}_3\text{N}_4$ products were obtained.

2.3 Preparation of SiO_2

In the synthesis of SiO_2 , the 10 mL of precursor tetraethyl ortho silicate (TEOS) was added dropwise into a solution of 5 mL of 2-propyl alcohol and 5.6 mL of water by sonication

for 45 min, in the addition of sodium hydroxide. The resulting mixture was stirred for 26 h at the room temperature. After reaction, the product was dried under vacuum at room temperature, and then the solid was washed with distilled water several times, and dried under vacuum at room temperature.

2.4 Fabrication of $\text{SiO}_2/\text{g-C}_3\text{N}_4$ Nanocomposite

The $\text{SiO}_2/\text{g-C}_3\text{N}_4$ nanocomposite was tailored via a simple solvothermal method. In 0.5 g of SiO_2 suspension was dispersed in 20 mL of deionised water and 15 mL of ethanol. Then, equal amount of 0.5 g of metal-free $\text{g-C}_3\text{N}_4$ was added in 10 mL of water separately and then two reaction mixture solution was sonication for 30 min. The obtained homogeneous dispersed solution was transferred into a 100 mL Teflon-lined autoclave and sealed, which was heated at 130 °C for 12 h. After that the solution was cooled and the solid mixture was centrifuged. The resultant product was washed with deionized water and ethanol several times and dried at 70 °C for 8 h. Finally, the present study, different ratios of melamine viz 0.25, 0.75 and 1% were added to different amount of SiO_2 loaded $\text{g-C}_3\text{N}_4$.

2.5 Characterization of Photocatalyst

The crystal phase and crystallite size were characterized by XRD on a Bruker D8 Advance X-ray powder diffractometer with $\text{Cu-K}\alpha$ radiation ($\lambda = 1.540598 \text{ \AA}$) in the angular range of 10°–80° (2θ) with an accelerating voltage of 40 kV and a current of 20 mA. SEM studies were used for the surface morphology of samples with a (Model SUPRA 40 Scanning Electron Microscope) acceleration voltage of 30 kV. Elemental analysis was examined by using {EDAX-Bruker Nano GmbH, X 50 Flash Detector (Model-5010)}. The bulk morphology, dispersion and distribution of SiO_2 in the $\text{g-C}_3\text{N}_4$ matrix were confirmed by transmission electron microscopy (TEM) using a Philips CM200. The photocatalyst was dispersed in 10 mL of ethanol by ultra sonication for 10 min and 250 mL of the sample solution was placed on a carbon coated copper grid. Then the grid was dried under infra-red light for 30 min before the TEM imaging. X-ray photoelectron spectroscopy (XPS) measurements were carried out using ULVAC-PHI 5000 Versa probe instrument. Shimadzu diffuse reflectance UV Vis-1800 spectrophotometer was used to analyze the absorption range and band gap energy of the samples. The absorption spectra in the photocatalytic process were monitored with a {Shimadzu 2600 UV-Vis} spectrophotometer. The FTIR spectra were recorded in transmission mode from 4000 to 400 cm^{-1} on a Shimadzu FTIR 8400 FTIR spectrometer using KBr discs.

2.6 Photocatalytic Activity of the $\text{SiO}_2/\text{g-C}_3\text{N}_4$ Photocatalyst

The photocatalytic activity of $\text{SiO}_2/\text{g-C}_3\text{N}_4$ nanocomposite was evaluated by RhB and CV 5 ppm dyes solution under visible light irradiation ($\lambda > 400 \text{ nm}$). 50 mg of photocatalyst of $\text{SiO}_2/\text{g-C}_3\text{N}_4$ nanocomposite was added to 75 mL of the dye solution in 150 mL reaction vessel. At a given time intervals, 5 mL of aliquots were collected and analyzed by recording the main absorption peaks for RhB and CV at 553 and 582 nm respectively. After the degradation, the catalyst was separated from the reaction mixture and dried to carry out the reusability tests. Prior to irradiation, the solutions were magnetically stirred in the dark condition for 1 h to ensure the equilibrium of the working solution. In a related system, the photocatalytic degradation of SiO_2 and $\text{g-C}_3\text{N}_4$ were furthermore been performed.

3 Results and Discussion

3.1 Structural Analysis

The crystalline nature and phase composition of the as synthesized SiO_2 , $\text{g-C}_3\text{N}_4$ and $\text{SiO}_2/\text{g-C}_3\text{N}_4$ nanocomposite was shown in Fig. 1. The XRD pattern of $\text{g-C}_3\text{N}_4$ depicts two distinctive diffraction peaks at around 2θ values at 12.8° and 27.5° were observed which corresponds to the (100) and (002) miller indices planes of hexagonal geometry of $\text{g-C}_3\text{N}_4$ respectively [JCPDS card no 87-1526] [40]. The typical XRD pattern of SiO_2 showed that the broad peak appeared at 2θ of around 23° corresponded to amorphous nature of SiO_2 [41]. The formation of $\text{SiO}_2/\text{g-C}_3\text{N}_4$ nanocomposite was

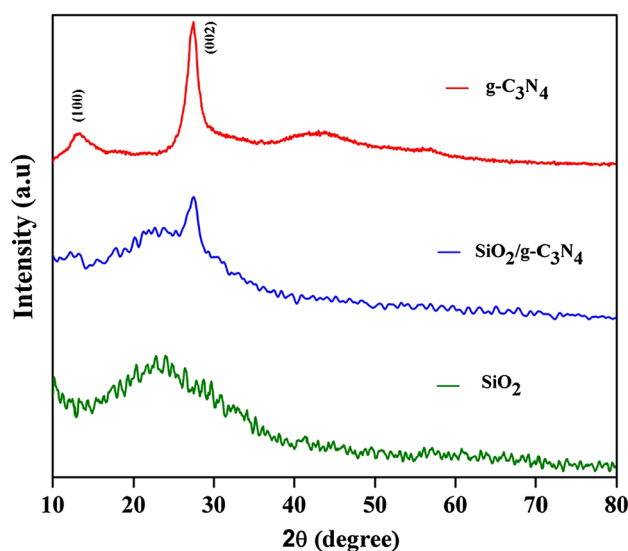


Fig. 1 XRD patterns of $\text{g-C}_3\text{N}_4$, SiO_2 , $\text{g-C}_3\text{N}_4/\text{SiO}_2$ nanocomposite

confirmed by XRD, it shows the characteristic peaks of both $g\text{-C}_3\text{N}_4$ and SiO_2 in $\text{SiO}_2/\text{C}_3\text{N}_4$ nanocomposite. However the average crystalline size of the $g\text{-C}_3\text{N}_4$ and $\text{SiO}_2/g\text{-C}_3\text{N}_4$ nanocomposite was calculated using Debye–Scherrer's formula [42, 43].

$$X_s = \frac{k\lambda}{\beta \cos \theta} \quad (1)$$

where X_s is the crystalline size, λ is the wavelength of the X-ray, β is the full width at half maximum (FWHM) of the diffraction peak, θ is the diffraction angle and k is the Scherrer's constant of the order of unity. The average crystalline size of the $g\text{-C}_3\text{N}_4$ and $\text{SiO}_2/g\text{-C}_3\text{N}_4$ nanocomposite is to be 78.31 and 36.29 nm respectively.

To investigate the structural information of $\text{SiO}_2/g\text{-C}_3\text{N}_4$ nanocomposite was further evidenced by FTIR analysis which is shown in Fig. S1. For pristine $g\text{-C}_3\text{N}_4$, sharpest and predominant peak at 809 cm^{-1} assigned to the breathing mode of tri-azine units [44] and the band in the $1200\text{--}1700\text{ cm}^{-1}$ were attributed to the typical stretching modes of C–N heterocycles [45, 46]. The characteristic peaks located at 1252, 1322, 1406, 1562 and 1653 cm^{-1} were assigned to the aromatic C–N stretching [47, 48]. In addition, to a minor peak at 2142 cm^{-1} ascribed to the accumulated double bond (indicating $\text{N}=\text{N}=\text{N}$ or $\text{N}=\text{C}=\text{N}$) additionally triple bond (indicating $\text{C}\equiv\text{N}$) of pristine $g\text{-C}_3\text{N}_4$. The FTIR spectra of SiO_2 showed the bands at 809 and 1109 cm^{-1} is assigned as the bending vibration of Si–OH and stretching vibration of Si–O–Si, respectively [49]. Furthermore, the two prominent characteristic peaks at 1632 and 3450 cm^{-1} belongs to the bending and stretching vibrations of the adsorbed water molecules on the surface. The broad band at 3140 cm^{-1} is attributed to the surface hydroxyl group which may be due to the moisture adsorption [50]. The peak mentioned above was shifted to higher region upon incorporation of SiO_2 in to the $g\text{-C}_3\text{N}_4$ matrix.

3.2 Morphological Analysis

The surface morphology and size of the $\text{SiO}_2/g\text{-C}_3\text{N}_4$ nanocomposite was studied by SEM analysis as shown in Fig. 2, a showed the SEM micrographs of the pure $g\text{-C}_3\text{N}_4$ which displays the plenty of nanosheets with an aggregated structure. The SEM micrographs (Fig. 2b) of SiO_2 sample is displays the cubic-like structure with an average particle size is to be 300 nm. It was clearly exhibited that the cubic like SiO_2 particles were well dispersed on the surface of $g\text{-C}_3\text{N}_4$ matrix (see Fig. 2c, d).

The surface morphology and size of the particle of as synthesized $\text{SiO}_2/g\text{-C}_3\text{N}_4$ nanocomposite were further investigated using TEM analysis which was displayed in Fig. 3. Figure 3a TEM images of as synthesized $g\text{-C}_3\text{N}_4$ showed a sheet-like morphology and well smooth surfaces. The TEM

images of SiO_2 clearly indicated that cubic like structure with some irregular structural morphology and the size was ranges from 20 to 30 nm which was illustrated in Fig. 3b. Interestingly, the TEM images of $\text{SiO}_2/g\text{-C}_3\text{N}_4$ composite revealed nanocube-like structure of SiO_2 which randomly anchored on the surface of $g\text{-C}_3\text{N}_4$ sheets which is shown in Fig. 3c. Figure 3d showed the selected-area emission diffraction (SAED) pattern revealed that the $\text{SiO}_2/g\text{-C}_3\text{N}_4$ cubes were indexed to the reflection plane of (100) and (002) orientation which is concurring with the XRD results (Scheme 1).

3.3 Surface Area Analysis

The Brunauer–Emmett–Teller (BET) specific surface area of the as-synthesized $g\text{-C}_3\text{N}_4$ and $\text{SiO}_2/g\text{-C}_3\text{N}_4$ nanocomposite were analyzed by N_2 adsorption–desorption isotherms which is shown in Fig. 4. The isotherms of as synthesized nanomaterials exhibited the type IV according to the IUPAC classification with a strong uptake is observed at high relative pressures ($P/P_0 > 0.9$) [51]. The BET surface area of the pure $g\text{-C}_3\text{N}_4$ and $\text{SiO}_2/g\text{-C}_3\text{N}_4$ was measured to be 45.05 and $58.12\text{ m}^2/\text{g}$ respectively. The surface area of the $\text{SiO}_2/g\text{-C}_3\text{N}_4$ nanocomposite was higher than that of $g\text{-C}_3\text{N}_4$. The large specific area of the $\text{SiO}_2/g\text{-C}_3\text{N}_4$ nanocomposite can accommodate more catalytic active sites and facilitates the transport of photogenerated charge carriers which could be lead to the superior photocatalytic performance [52].

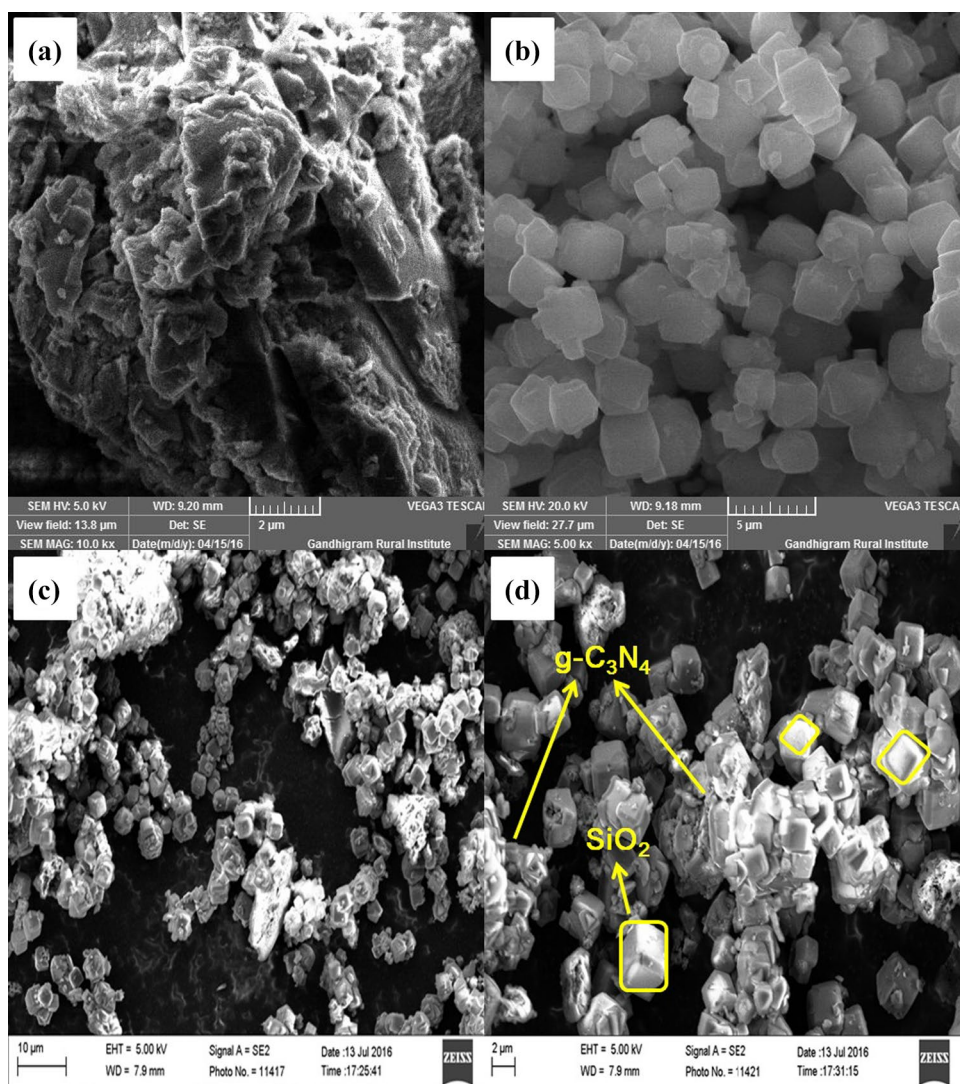
3.4 EDAX and Elemental Mapping Analysis

The compositions of elements present in the synthesized $g\text{-C}_3\text{N}_4$, SiO_2 and $\text{SiO}_2/g\text{-C}_3\text{N}_4$ nanocomposite was examined by EDX analysis and which is shown in Fig. S2. Figure S2a, b show the EDX spectra of as-prepared $g\text{-C}_3\text{N}_4$, and SiO_2 nanocubes which mainly composed C, N and Si, O elements respectively. The EDX results $\text{SiO}_2/g\text{-C}_3\text{N}_4$ nanocomposite was shown in Fig. 6c. The EDX analysis clearly indicated that $\text{SiO}_2/g\text{-C}_3\text{N}_4$ nanocomposites consist of only C, N, Si and O and their weight percentages is 56.34, 22.99, 6.18 and 14.49% respectively. There is no other elements were found in the $\text{SiO}_2/g\text{-C}_3\text{N}_4$ nanocomposites. Figure S3 shows the composition of the elements present in the $\text{SiO}_2/g\text{-C}_3\text{N}_4$ nanocomposite was clearly evidenced by elemental mapping analysis. These results strongly confirmed the presence of carbon, nitrogen, oxygen, and silica is uniformly distributed in the $\text{SiO}_2/g\text{-C}_3\text{N}_4$ nanocomposites.

3.5 XPS Analysis

X-ray photoelectron spectroscopy was used to determine the chemical composition and chemical states of the synthesized $\text{SiO}_2/g\text{-C}_3\text{N}_4$ nanocomposites which is illustrated in Fig. 5.

Fig. 2 SEM micrographs of **a** g-C₃N₄, **b** SiO₂, **c**, **d** SiO₂/g-C₃N₄ nanocomposite



The XPS survey spectrum in Fig. 5a displays the existence of C, N, Si and O elements and which is well consistent with EDX results. As displayed in Fig. 5b, the symmetric XPS peak of C1s located at 287.41 eV which can be attributed to the core level of g-C₃N₄ [53]. The peak at 399.12 eV can be ascribed to the sp³ bonded N atoms [54]. Figure 5c, showed the Si 2*p* binding energy of SiO₂ peak, centered at 103.48 eV which confirm the chemical bond between g-C₃N₄ and SiO₂ [55]. The O1s spectrum observed at a strong intense peak of 532.33 eV, corresponding to the lattice oxygen of O²⁻ oxidation state in the SiO₂ nanomaterials which is shown in Fig. 5d [56]. Hence, this kind of bond is conducive to the successful formation of SiO₂/g-C₃N₄ nanocomposites.

3.6 Optical Properties

The photoluminescence (PL) spectrum is a useful tool for determining the transfer, migration and recombination behavior of photogenerated charged carriers of

nanomaterials [57, 58] and relative results are depicted in Fig. S4. The PL emission is mainly due to the photogenerated charged carriers in a semiconductor, reveals that higher PL intensity indicates a higher recombination rate in contrast and a lower PL intensity expresses a lower recombination rate [13, 59]. The as synthesized PL intensity of g-C₃N₄ with high emission bands centered at 460 nm ascribed to the energy gap recombination of charge carriers, which identifies that photoinduced electron hole recombination rate was high on g-C₃N₄. However, it can be found that PL intensity of SiO₂/g-C₃N₄ nanocomposite is lower intensity when compared to pristine g-C₃N₄, which may be due to the SiO₂ nanocubes are successfully inserted with the g-C₃N₄ matrix. This reason may be imply that the shrink recombination rate of the electron–hole pair charge carrier is in the SiO₂/g-C₃N₄ nanocomposite [60, 61]. In addition, the lower PL intensity of SiO₂/g-C₃N₄ nanocomposite was visibly expressed that slower electron hole recombination rate which was better for the photocatalytic activity.

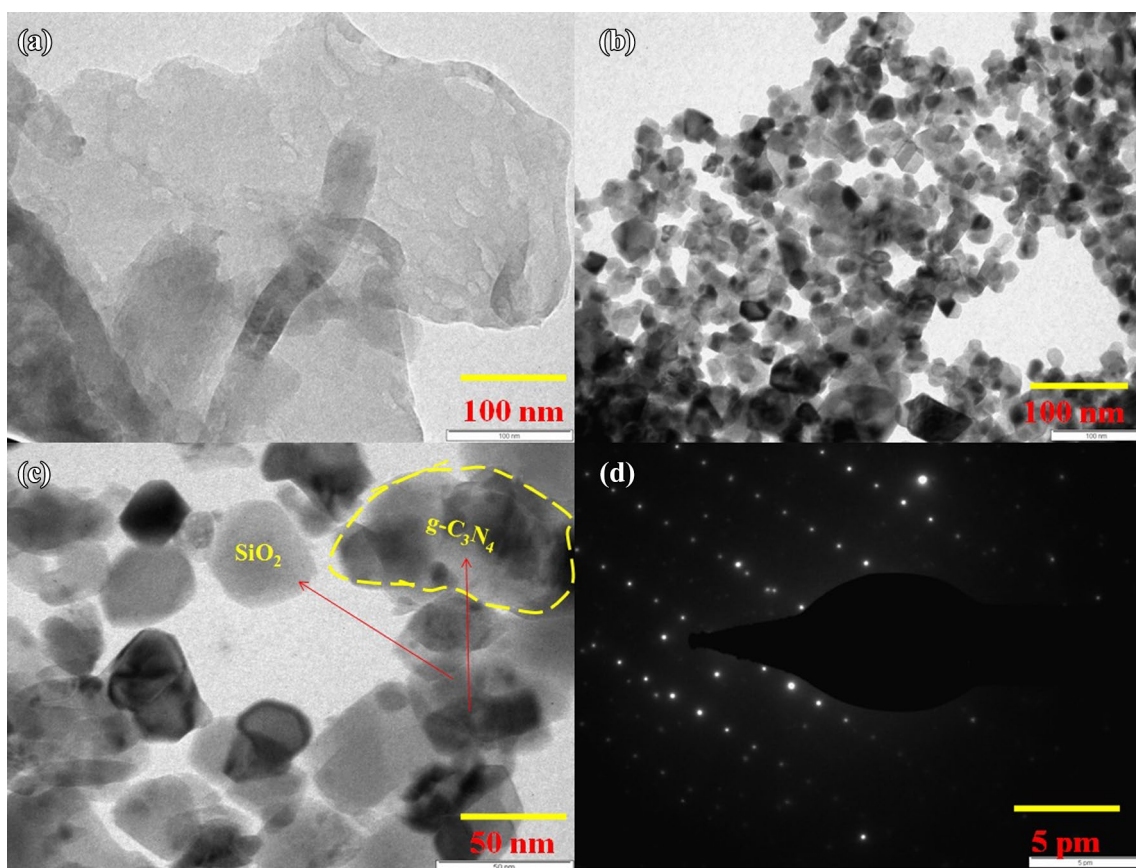
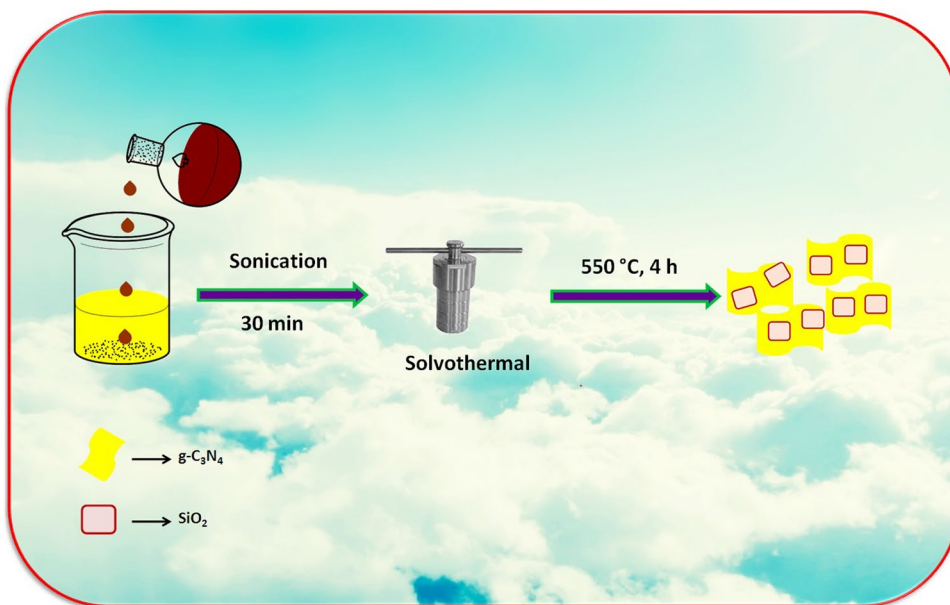


Fig. 3 TEM images of **a** g-C₃N₄, **b** SiO₂, **c** SiO₂/g-C₃N₄ nanocomposite, **d** corresponding SAED pattern

Scheme 1 Schematic diagram of synthesis of SiO₂/g-C₃N₄ nanocomposite



The optical absorption properties of the SiO₂/g-C₃N₄ nanocomposite are significant parameter for the selection of right kind of light needed for the photocatalytic degradation

of organic dye solution [62]. The DRS mode UV–Visible absorption spectra of pristine g-C₃N₄, SiO₂ and SiO₂/g-C₃N₄ nanocomposite were measured and the result is shown in

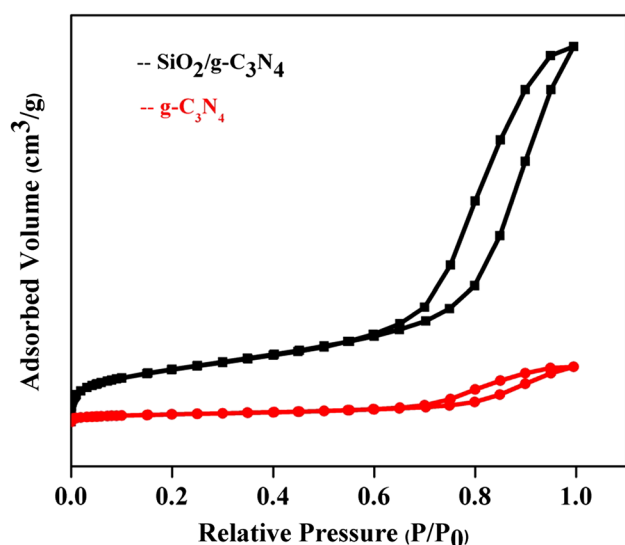


Fig. 4 The BET surface area calculated from N_2 adsorption–desorption isotherms

Fig. S5. The pristine $g-C_3N_4$ photoabsorption in the UV light to visible light region 477 nm, which corresponds to the direct and indirect band gaps of 2.73 and 2.70 eV, respectively. The pure SiO_2 showed the weaker light photoabsorption ability. The $SiO_2/g-C_3N_4$ nanocomposite showed the blue shift in the optical absorption edge in the visible light region around at 448 nm, which was related to the direct and indirect band gaps of $SiO_2/g-C_3N_4$ at about 2.76 and 2.67 eV, respectively. The band gap value calculations for the $g-C_3N_4$ and $SiO_2/g-C_3N_4$ nanocomposite results were Kubelka–Munk and Tauc plots and calculated by the energy gap value using the following equation,

$$\alpha h\nu = \beta(h\nu - E_g)^n$$

where E_g is the band gap energy of semiconductor, β is the absorption constant, α is the absorption coefficient. The index n has numerous values of 1/2, 2, 3/2 and 3 for allowed direct and indirect, forbidden direct and indirect different electronic transitions respectively [63].

3.7 Photocatalytic Activity of $SiO_2/g-C_3N_4$ Nanocomposite

Photocatalytic activity of as-synthesized $SiO_2/g-C_3N_4$ nanocomposite was evaluated towards the photodegradation of RhB and CV dyes under visible light irradiation. Figure 6a, b exhibit the absorption spectra of an aqueous solution of RhB and CV (556 and 582) dyes for the photodegradation profiles as a function of irradiation time. It can be seen that, the illumination of dye solution in the presence of photocatalyst leads to drastically decrease in absorption intensity with

increasing the irradiation. The color of the dye solutions were entirely disappears at 70 and 90 min, and the intensity of other small peaks is also decreased. After the degradation process, the photocatalyst was separated from the reaction mixture by centrifugation, washed with DI water and dried for the carry out reusability test.

3.8 Effect of Initial RhB and CV Dye Concentration

The effect of initial concentration of RhB and CV dye solutions on the photodegradation rate was measured by varying the dye concentration from 5 to 20 ppm which is shown in Fig. S6. The rate of dye degradation was decreased with increasing the concentration of RhB and CV dye solution. It was observed that the 5 ppm dye concentration of dye solution was greatly degraded, and further increasing of concentration the rate was falls down. Furthermore, increasing the initial concentration of dye solution, more number of organic molecules was present in the dye solution, which is adsorbed on the catalyst surface. In other words, the photogeneration of charge carries was significantly reduced and in turn the dye degradation is reduced due to the lack of oxidizing species.

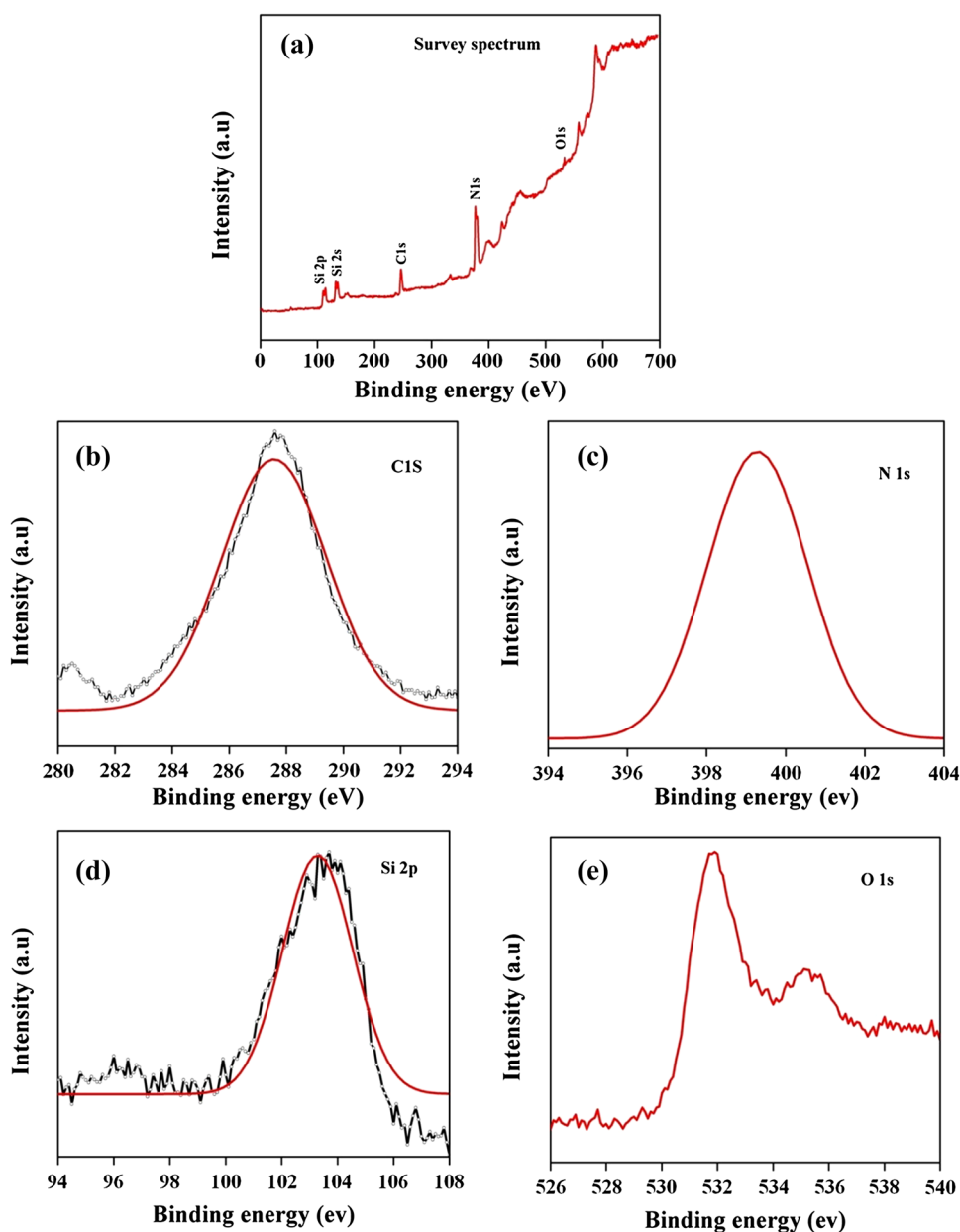
3.9 Effect of Catalyst Weight

Figure S7 shows the effect of catalyst weight on photocatalytic degradation of RhB and CV dyes in the presence of $SiO_2/g-C_3N_4$ nanocomposite was assessed by varying the amount of catalyst weight from 10 to 75 mg. The increment of 50 mg of photocatalyst results the highest photodegradation efficiency compared to other photocatalyst (10, 25, 75 mg). The rate of photodegradation was decreased after the 50 mg amount of catalyst which might be due to that the penetration of light becomes which may be due to the lower efficiency of the composite. Therefore, the particles also tent to source agglomerate under these conditions reduced the accessibility of both dye molecules and radiation to the active sites of the catalyst surface to contribute in the photodegradation process [64].

3.10 Effect of Different pH

The photodegradation of dye solutions were performed in the different pH values were estimated which is depicted in Fig. S8. The effect of pH values on degradation of the dye solutions was evaluated by varying the pH values from 2 to 12 (2, 4, 8, 10 and 12) which adjusted by adding very dilute solution of hydrochloric acid or sodium hydroxide. The degradation rate was slightly quick for the photodegradation of two dye solution during in the acidic pH (2–6). Hence, in the acidic medium the surface charge of the photocatalyst might be influenced [65, 66]. Moreover, due to the generation of

Fig. 5 XPS spectra of the SiO₂/C₃N₄ nanocomposite: **a** survey, **b** C1s, **c** N1s, **d** Si 2p, (e) O1s



alternative number of hydroxyl radical ($\bullet\text{OH}$) in the acidic medium was much easier. It was observed that photocatalytic activity was decreased at alkaline pH while it was very difficult for the generation of $\bullet\text{OH}$ in the alkaline medium compared to neutral and acidic conditions [67]. However, the efficiency of photodegradation rate was higher at neutral and acidic pH values while compare to basic medium.

3.11 Detection of Reactive Oxidative Species (ROS)

The active involvement of reactive oxidative species such as $\bullet\text{OH}$ and $\text{O}_2^{\bullet-}$ during the photodegradation of RhB and CV dyes were identified by using radical trapping experiments. In this present system, azide ion (AZ), benzoic acid

(BA), triphenylphosphine (TPP) and acryl amide (AA) were used as scavengers and the results are depicted as shown in Fig. S9. In general, AZ, AA and TPP is a singlet oxygen quencher which were used as the scavenger for superoxide radical anion ($\text{O}_2^{\bullet-}$) [67–70]. From the Fig. S9, there was no significant reduction of degradation rate was observed for the both RhB and CV dyes upon the addition of AZ. Furthermore, the addition of AA and TPP could slightly decrease the photodegradation efficiency which suggests that minor active involvement of $\text{O}_2^{\bullet-}$. On contrarily, BA is the hydroxyl ion ($\bullet\text{OH}$) scavenger that scavenge the $\bullet\text{OH}$ radicals during the photocatalytic reaction [71]. The results showed that the addition of BA in the present photocatalytic reaction slow down the rate of degradation above 90%,

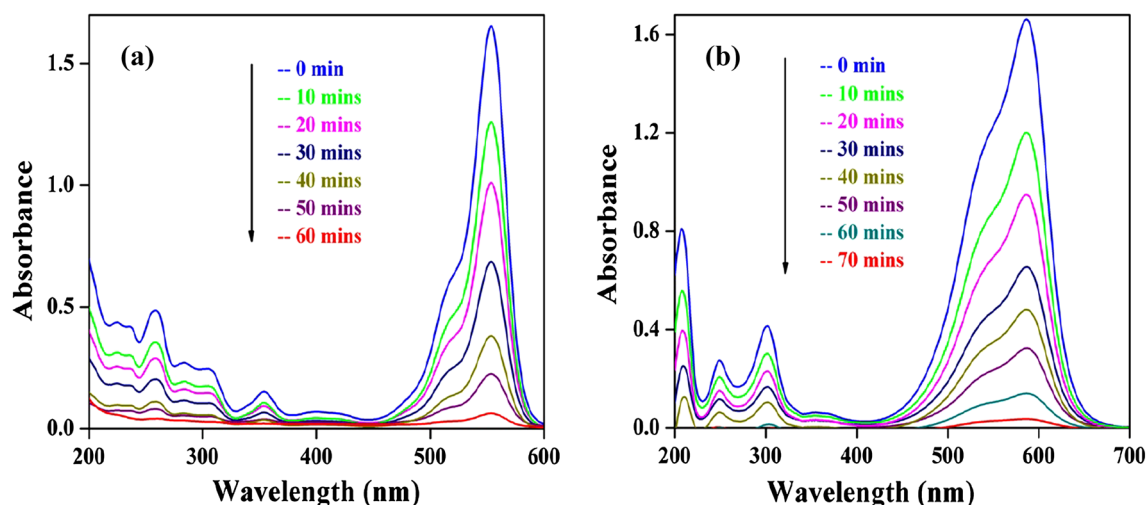
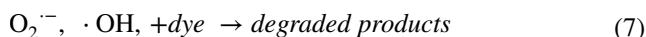
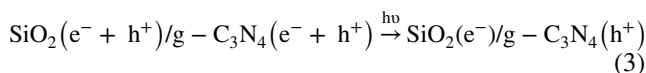
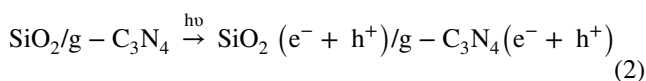


Fig. 6 Absorption spectra of **a** RhB and **b** CV dye solutions irradiated under visible light in the presence of 50 mg of $\text{SiO}_2/\text{g-C}_3\text{N}_4$ nanocomposite

which clearly suggests that the degradation facilitates by the $\bullet\text{OH}$ radical produced from the electron–hole pairs of the photocatalyst. Hence, the results concluded that $\bullet\text{OH}$ radicals plays major dynamic role and $\text{O}_2^{\bullet-}$ plays a minor role for the efficient photodegradation of both RhB and CV dyes.

3.12 Plausible Mechanism

The mechanism for the photodegradation of the organic dyes in the presence of $\text{SiO}_2/\text{g-C}_3\text{N}_4$ can be illustrated as follows,



When a prepared photocatalyst was irradiated by visible light, the excited electrons (e^-) from the conduction band (CB) of $\text{SiO}_2/\text{g-C}_3\text{N}_4$ nanocomposite to the valance band and leaving holes (h^+) as shown in Eqs. (2) and (3). Then, the electron will react with the oxygen molecule to form a superoxide radical anion ($\text{O}_2^{\bullet-}$) Eq. (4), While the conduction electron (e^-) which reacted with H^+ and O_2 , to form oxidizing agent (H_2O_2) Eq. (5). Moreover, the H_2O_2 reacts with superoxide radical anion it formed the $\bullet\text{OH}$ radical behind

formation of another ROS Eq. (6). Finally, $\bullet\text{OH}$ radical and super oxide radical anion was involved in the visible light facilitated the photocatalytic degradation of the dye solution.

3.13 Reusability and Stability of the Catalyst

The reusability and stability of $\text{SiO}_2/\text{g-C}_3\text{N}_4$ photocatalyst is crucial a factor for its practical application and therefore, the reusability experiments were carried and the results as represented in Fig. S10a. The $\text{SiO}_2/\text{g-C}_3\text{N}_4$ nanocomposite showed the 95% dye degradation efficiency of RhB in its second recycle run and after the 3rd cycle run of photocatalyst was the activity was slightly decreased and 93% of dye degradation. It was observed that, above 90% of degradation were achieved even after fifth usage. In addition, Fig. S10b shows the SEM images of $\text{SiO}_2/\text{g-C}_3\text{N}_4$ nanocomposite before and after photocatalytic reaction. The SEM images of $\text{SiO}_2/\text{g-C}_3\text{N}_4$ nanocomposite after fifth cycle, the photocatalyst were slightly aggregated and homogeneously distributed on the $\text{g-C}_3\text{N}_4$ surface. These results suggested that the $\text{SiO}_2/\text{g-C}_3\text{N}_4$ nanocomposite were exhibits excellent stability for the degradation of RhB and CV dyes.

4 Conclusions

In conclusion, we developed a novel solvothermal route for the synthesis of $\text{SiO}_2/\text{g-C}_3\text{N}_4$ nanocomposite. The FT-IR, XPS, BET, UV-DRS, EDX spectra and PL analysis results showed the SiO_2 was successfully decorated with $\text{g-C}_3\text{N}_4$ matrix. The as-synthesized $\text{SiO}_2/\text{g-C}_3\text{N}_4$ nanocomposite had superior degradation performance. Both RhB and CV dyes under visible light illumination predicted the degradation

rate 98% within 60 min and 97% within 70 min respectively. Moreover, the $\text{SiO}_2/\text{g-C}_3\text{N}_4$ composite photocatalyst also showed excellent photocatalytic stability and reusability. It is revealed that the $\text{SiO}_2/\text{g-C}_3\text{N}_4$ nanocomposite would be a potential candidate for treatment of RhB and CV dyes containing waste water.

Acknowledgements The authors express their sincere thanks to the College managing board, Principal and Head of the Department, VHNSN College for providing the necessary research facilities. Finally I thank Padova University, Italy for providing XPS analysis facility.

References

- D.A. Gopakumar, D. Pasquini, M.A. Henrique, L.C. Morais, Y. Grohens, S. Thomas, *ACS Sustain. Chem. Eng.* **5**, 2026 (2017)
- S. Wojtyla, W. Macyk, T. Baran, *Photochem. Photobiol. Sci.* **16**, 1079 (2017)
- Y. Hanifehpour, B. Mirtamizdoust, M.A. Cheney, S.W. Joo, *J. Mater. Sci.* **28**, 11654 (2017)
- K.R. Reddy, K.V. Karthik, S.B. Benaka Prasad, S.K. Soni, H.M. Jeong, A.V. Raghu, *Polyhedron* **120**, 169 (2016)
- R. Karthik, J.V. Kumar, S.M. Chen, K. Chelladurai, Y.H. Cheng, V. Muthuraj, *ACS Appl. Mater. Interfaces* **9**, 6547 (2017)
- K.R. Reddy, K. Nakata, T. Ochiai, T. Murakami, D.A. Tryk, A. Fujishima, *J. Nanosci. Nanotechnol.* **11**, 3692 (2011)
- M. Cakici, K.R. Reddy, F.A. Marroquin, *Chem. Eng. J.* **309**, 151 (2017)
- J. Zhu, P. Xiao, H. Li, S.A.C. Carabinerio, *ACS Appl. Mater. Interfaces* **6**, 16449 (2014)
- X. Chen, B. Zhou, S. Yang, H. Wu, Y. Wu, L. Wu, J. Pan, X. Xiong, *RSC Adv.* **5**, 68953 (2015)
- Q. Chen, H. Hou, D. Zhang, S. Hu, T. Min, B. Liu, C. Yang, W. Pu, J. Hu, J. Yang, *J. Photochem. Photobiol. A* **350**, 1 (2018)
- S. Zhang, J. Li, M. Zeng, J. Li, J. Xu, X. Wang, *Chem. Eur. J.* **20**, 9805 (2014)
- Y. Yao, Y. Cai, F. Lu, J. Qin, F. Wei, C. Xu, S. Wang, *Ind. Eng. Chem. Res.* **53**, 17294 (2014)
- S. Samanta, S. Martha, K. Parida, *ChemCatChem* **6**, 1453 (2014)
- H. Fujiwara, H. Hosokawa, K. Murakoshi, Y. Wada, S. Yanagida, T. Okada, H. Kobayashi, *J. Phys. Chem. B* **101**, 8270 (1997)
- A. Dhakshinamoorthy, S. Navalon, A. Corma, H. Garcia, *Energy Environ. Sci.* **5**, 9217 (2012)
- X. Wang, S. Blechert, M. Antonietti, *ACS Catal.* **2**, 1596 (2012)
- K. Maeda, X. Wang, Y. Nishihara, D. Lu, M. Antonietti, K. Domen, *J. Phys. Chem. C* **113**, 4940 (2009)
- H. Yan, H. Yang, *J. Alloys Compd.* **509**, 26 (2011)
- X.C. Wang, K. Maeda, X.F. Chen, K. Takanebe, K. Domen, Y. Hou, X. Fu, M. Antonietti, *J. Am. Chem. Soc.* **131**, 1680 (2009)
- F. Dong, Y. Li, Z. Wang, W.K. Ho, *Appl. Surf. Sci.* **358**, 393 (2015)
- X.F. Chen, J.S. Zhang, X.Z. Fu, M. Antonietti, X.C. Wang, *J. Am. Chem. Soc.* **131**, 11658 (2009)
- M. Zhang, J. Xu, R.L. Zong, Y.F. Zhu, *Appl. Catal. B* **147**, 229 (2014)
- G.H. Dong, K. Zhao, L.Z. Zhang, *Chem. Commun.* **48**, 6178 (2012)
- X.C. Wang, X.F. Chen, A. Thomas, X.Z. Fu, M. Antonietti, *Adv. Mater.* **21**, 1609 (2009)
- B.J. Jankiewicz, D. Jamiola, J. Choma, M. Jaroniec, *Adv. Colloid Interface Sci.* **170**, 28 (2012)
- S.K. Samantaray, K.M. Parida, *Appl. Catal. A* **211**, 175 (2001)
- H.B. Yener, S.S. Helvaci, *Sep. Purif. Technol.* **140**, 84 (2015)
- A. Showkat, Y. Zhang, M.S. Kim, A.I. Gopalan, K.R. Reddy, K.P. Lee, *Bull. Korean Chem. Soc.* **28**, 1985 (2007)
- Y. Zhang, Y. Li, Z. Wang, K. Zhao, *Nano Lett.* **14**, 7161 (2014)
- Y.P. Zhang, S.H. Lee, K.R. Reddy, A.I. Gopalan, K.P. Lee, *J. Appl. Polym. Sci.* **104**, 2743 (2007)
- K.K. Qian, R.H. Bogner, *J. Pharm. Sci.* **101**, 444 (2012)
- R.H. Dave, Overview of pharmaceutical excipients used in tablets and capsules. *Drug Topics* (online). Advanstar. 10/24/2008
- Y. Wu, L. Tao, J. Zhao, X. Yue, W. Deng, Y.X. Li, C. Wang, *Res. Chem. Intermed.* **42**, 3609 (2016)
- J. Lei, Y. Chen, F. Shen, L.Z. Wang, Y.D. Liu, J.L. Zhang, *J. Alloys Compd.* **631**, 328 (2015)
- W. Wang, J.C. Yi, D. Xia, P.K. Wong, Y. Li, *Environ. Sci. Technol.* **47**, 8724 (2013)
- J.X. Sun, Y.P. Yuan, L.G. Qin, X. Jiang, A.J. Xie, Y.H. Shen, J.F. Zhu, *Dalton Trans.* **41**, 6756 (2012)
- J. Wang, Z. Guan, J. Huang, Q. Li, J. Yang, *J. Mater. Chem. A* **2**, 7960 (2014)
- Y. Wang, X. Bai, C. Pan, J. He, Y. Zhu, *J. Mater. Chem.* **22**, 11568 (2012)
- K. Prakash, P.S. Kumar, P. Latha, K.S. Durai, R. Shanmugam, S. Karuthapandian, *Mater. Res. Bull.* **93**, 112 (2017)
- J.H. Liu, T.K. Zhang, Z.C. Wang, G. Dawson, W. Chen, *J. Mater. Chem.* **21**, 14398 (2011)
- X. Wang, S. Wang, W. Hu, J. Gai, L. Zhang, L. Dong, L. Zhao, Y. He, *Mater. Lett.* **115**, 53 (2014)
- K.R. Reddy, K.P. Lee, A.G. Iyengar, *J. Appl. Polym. Sci.* **104**, 4127 (2007)
- K.R. Reddy, V.G. Gomes, M. Hassan, *Mater. Res. Express* **1**, 015012 (2014)
- X. Bai, C. Sun, S. Wu, Y. Zhu, *J. Mater. Chem. A* **3**, 2741 (2015)
- S. Zhang, J. Li, M. Zeng, G. Zhao, J. Xu, W. Hu, X. Wang, *ACS Appl. Mater. Interfaces* **5**, 12735 (2013)
- Y. Hu, M. Xie, S. Huang, H. Xu, H. Ji, J. Xia, Y. Li, H. Li, *RSC Adv.* **5**, 26281 (2015)
- X. Yuan, C. Zhou, Y. Jin, Q. Jing, Y. Yang, X. Shen, Q. Tang, Y. Mu, A.K. Du, *J. Colloid Interface Sci.* **468**, 211 (2016)
- K.R. Reddy, K.P. Lee, A.I. Gopalan, *Colloid Surf. A* **320**, 49 (2008)
- X.M. Tai, Z.P. Du, W.X. Wang, M.F. Hou, Y.H. Zhao, *Power Technol.* **264**, 273 (2014)
- T. Wang, X.Q. Yan, S.S. Zhao, B. Lin, C. Xue, G.D. Yang, S.J. Ding, B.L. Yang, C.S. Ma, G. Yang, G.R. Yang, *J. Mater. Chem. A* **2**, 15611 (2014)
- J.Y. Zhang, Y.H. Wang, J. Jin, J. Zhang, Z. Lin, F. Huang, J.G. Yu, *ACS Appl. Mater. Interfaces* **5**, 10317 (2013)
- Q. Liang, M. Zhang, C. Yao, C. Liu, S. Xu, Z. Li, J. Photochem. Photobiol. A **332**, 357 (2017)
- J. Ma, D. Huang, W. Zhang, J. Zou, Y. Kong, J. Zhu, S. Komarneni, *Chemosphere* **162**, 269 (2016)
- W. Zhang, X. Xiao, Y. Li, X. Zeng, L. Zheng, C. Wan, *Appl. Surf. Sci.* **389**, 496 (2016)
- C.Q. Li, Z. Sun, X. Li, L. Liu, S. Zheng, *Adv. Powder Technol.* **27**, 2051 (2016)
- M.E. Pilleux, C.R. Grahmann, V.M. Fuenzalida, *J. Am. Ceram. Soc.* **77**, 1601 (1994)
- M. Jeem, L. Zhang, J. Ishioka, T. Shibayama, T. Iwasaki, T. Kato, S. Watnanabe, *Nano Lett.* **17**, 2088 (2017)
- H. Hassan, E. Haque, K.R. Reddy, A.I. Minett, J. Chen, V.G. Gomes, *Nanoscale* **6**, 11988 (2014)
- K. Li, S. Gao, Q. Wang, H. Xu, Z. Wang, B. Huang, Y. Dai, J. Lu, *ACS Appl. Mater. Interfaces* **7**, 9023 (2015)
- S.Y. Chou, C.C. Chen, Y.M. Dai, J.H. Lin, W.W. Lee, *RSC Adv.* **6**, 33478 (2016)

61. A. Akhundi, A.H. Yangjeh, *J. Colloid Interface Sci.* **482**, 165 (2016)
62. K.R. Reddy, B.C. Sin, C.H. Yoo, W. Park, K.S. Ryn, J.S. Lee, D. Sohn, Y. Lee, *Scripta Mater.* **58**, 1010 (2008)
63. S. Wojtyla, T. Baran, *J. Inorg. Organomet. Polym.* **27**, 436 (2017)
64. Y. Hanifehpour, N. Hamnabard, B. Mirtamizdoust, S.W. Joo, *J. Inorg. Organomet. Polym.* **26**, 623 (2016)
65. P. Latha, R. Dhanabackialakshmi, P.S. Kumar, S. Karuthapandian, *Sep. Purif. Technol.* **168**, 124 (2016)
66. P.S. Kumar, S. Sobiya, M. Selvakumar, S.G. Babu, S. Karuthapandian, *Energy Environ. Focus* **5**, 139 (2016)
67. K. Saravanakumar, M. Ramjan, P. Suresh, V. Muthuraj, *J. Alloys Compd.* **664**, 149 (2016)
68. W. Lei, D. Portehault, R. Dimova, M. Antonietti, *J. Am. Chem. Soc.* **133**, 7121 (2011)
69. V.N. Khabashesku, J.L. Zimmerman, J.L. Margrave, *Chem. Mater.* **12**, 3264 (2000)
70. X. Zhang, F. Wu, N. Deng, *J. Hazard. Mater.* **85**, 117 (2011)
71. P.S. Kumar, S. Karuthapandian, M. Umadevi, A. Elangovan, V. Muthuraj, *Mater. Focus* **5**, 128 (2016)